Agricultural and Forest Meteorology 291 (2020) 108041

Contents lists available at ScienceDirect

Agricultural and Forest Meteorology

journal homepage: www.elsevier.com/locate/agrformet

# Patterns in the spectral composition of sunlight and biologically meaningful spectral photon ratios as affected by atmospheric factors

T. Kotilainen[a,b,*], PJ. Aphalo[a], CC. Brelsford[a], H. Böök[c], S. Devraj[d], A. Heikkilä[c], R. Hernández[e], A. Kylling[f], AV. Lindfors[c], TM. Robson[a]

[a] Organismal and Evolutionary Biology (OEB), Viikki Plant Science Centre (ViPS), Faculty of Biological and Environmental Sciences, University of Helsinki, Finland
[b] Current address: Natural Resources Institute Finland, Turku, Finland
[c] Finnish Meteorological Institute, Helsinki, Finland
[d] Renewable Energy Technologies Division, The Energy and Resources Institute, New Delhi, India
[e] Department of Horticultural Science, NC State University, Raleigh, NC, USA
[f] NILU – Norwegian Institute for Air Research, Kjeller, Norway

ARTICLE INFO

*Keywords:*
Spectral photon ratios
Water-vapour column
Total ozone
Aerosol optical depth
Radiative transfer
Plant photobiology

ABSTRACT

Plants rely on spectral cues present in their surroundings, generated by the constantly changing light environment, to guide their growth and reproduction. Photoreceptors mediate the capture of information by plants from the light environment over a wide range of wavelengths, but despite extensive evidence that plants respond to various light cues, only fragmentary data have been published showing patterns of diurnal, seasonal and geographical variation in the spectral composition of daylight. To illustrate patterns in spectral photon ratios, we measured time series of irradiance spectra at two distinct geographical and climatological locations, Helsinki, Finland and Gual Pahari, India. We investigated the drivers behind variation of the spectral photon ratios measured at these two locations, based on the analysis of over 400 000 recorded spectra. Differences in spectral irradiance were explained by different atmospheric factors identified through multiple regression model analysis and comparison to spectral irradiance at ground level simulated with a radiative transfer model. Local seasonal and diurnal changes in spectral photon ratios were related to solar elevation angle, atmospheric water-vapour content and total ozone column thickness and deviated from their long-term averages to an extent likely to affect plant photobiology. We suggest that future studies should investigate possible effects of varying photon ratios on terrestrial plants. Solar elevation angle especially affects the patterns of B:G and B:R ratios. Water vapour has a large effect on the R:FR photon ratio and modelled climate scenarios predict that increasing global temperatures will result in increased atmospheric water vapour. The development of proxy models, utilising available data from weather and climate models, for relevant photon ratios as a function of solar elevation angle and atmospheric factors would facilitate the interpretation of results from past, present and future field studies of plants and vegetation.

## 1. Introduction

### 1.1. Light as a source of information for plants

Plants perceive changes in their environment and use them as sources of information; as cues and signals, allowing them to pre-emptively acclimate to impending changes in resources and in doing so often enhance their fitness (Aphalo and Ballaré, 1995; Casal, 2013; Chamovitz, 2018). Solar radiation is one such variable perceived by plants which carries information about the environment. Responses of plants to the red (R), far-red (FR), blue (B), green (G) and ultraviolet (UV) components of solar and artificial radiation have been studied for several decades, leading to the identification of more than a dozen plant photoreceptors grouped into five families: phytochromes (PHYs), cryptochromes (CRYs), phototropins (PHOTs), zeitlupe proteins (ZEITs), and UV RESISTANCE LOCUS 8 (UVR8). Each of these families of photoreceptors predominantly absorbs a certain range of wavelengths and responses are coordinated by a downstream signalling network controlling gene expression, metabolism, whole-plant responses and plant-plant interactions (Casal, 2013; Goyal et al., 2013).

* Corresponding author at: Organismal and Evolutionary Biology (OEB), Viikki Plant Science Centre (ViPS), Faculty of Biological and Environmental Sciences, University of Helsinki, Finland and Natural Resources Institute Finland, Turku, Finland.
*E-mail address:* titta.kotilainen@luke.fi (T. Kotilainen).

https://doi.org/10.1016/j.agrformet.2020.108041
Received 6 September 2019; Received in revised form 14 May 2020; Accepted 20 May 2020

The ability to synchronise growth and dormancy according to seasonal variation in the climatic conditions is of paramount importance to plants; with photoperiod central to regulating these transitions (Vince-Prue et al., 2001; Welling and Palva, 2006). Likewise, daylight irradiance and its spectral composition informs plants about objects and other plants in their neighbourhood (Ballare et al., 1987). The changing ratios of certain spectral integrals have been identified as controls on hypocotyl elongation using *Arabidopsis thaliana* seedlings grown under controlled conditions. In addition to the R:FR ratio, the B:G ratio can drive this process (Sellaro et al., 2010: higher ratio; shorter hypocotyl). The effects of blue and green light on growth responses associated with shade avoidance can be mediated through cryptochromes and it has been shown that the B:G ratio decreases with increasing vegetational shade (Sellaro et al., 2010). Further, evidence from greenhouse experiments suggest that a low blue to red ratio (B:R) accompanied by low daily accumulated PAR can result in differences in plant morphology and growth, typical of the shade avoidance syndrome (SAS) (Hernández and Kubota, 2014). A recent study has shown that photoreceptor interactions may also depend on the time of the day at which different light cues are sensed and on the duration of exposure to these cues (Sellaro et al., 2018). This builds on earlier research showing that plant growth and development is greatly affected by both changing plant spacing at different times of the day in sunlight (Casal et al., 1990) and by using brief end-of-day illumination treatments to alter the received spectrum immediately prior to the day-to-night transition (Aphalo et al., 1991; Chia and Kubota, 2010; Yang et al., 2012). Hence, interpretation of plants' photomorphogenic responses in sunlight from an ecological perspective requires knowledge of how spectral irradiance at ground level varies through the day and through seasons at different latitudes and under different atmospheric conditions.

### 1.2. Availability of time series data for the spectrum of sunlight at ground level

Compared to the well understood effect of vegetation on the light environment of neighbouring plants (Ballaré, 1999; Chelle et al., 2007; Flint and Caldwell, 1998; Grant et al., 2005; Smith, 1982), there is limited information about how the spectral irradiance at ground level is affected by local atmospheric factors at different solar elevation angles. Variation in the spectral composition of solar radiation above vegetation could provide additional cues to plants and/or alter spectral cues such as those related to shading.

Data available from measurements with pyranometers and scanning spectroradiometers at different locations, and derived photon ratios, are summarised in Table 1. The smallest R:FR photon ratios, between *c* 0.5 to 0.9, were recorded at low solar elevation angles between *c* -10° to 5° while the R:FR photon ratio was *c* 1.0-1.48 at high solar elevation angles. In addition, Hughes et al. (1984) and Lee and Downum (1991) reported high variability and/or increasing R:FR values around sunrise/sunset. Three studies reporting B:R photon ratio found similar trends (Hughes et al., 1984; Lee and Downum, 1991; Taulavuori et al., 2010), i.e. the ratio was below 1.0 during the daytime and increased up to *c* 3.0 when the sun was below the horizon.

There are relatively few published time series of spectral irradiance at ground level, measured with high frequency (tens of times per hour) over moderately long periods (months or years) together with detailed atmospheric data at the same site. Atmospheric composition has the greatest effect on the solar spectral irradiance at ground level when the solar disk is near the horizon and the path length of direct radiation through the atmosphere is longest. During twilight, the sun is below the horizon, but close to it so that the sky is illuminated. Before and during twilight, the daylight spectrum changes very rapidly making it necessary to acquire each whole spectrum within a very short time, or even better, acquire data for all wavelengths simultaneously. As explained above, this is a time of the day when light spectral composition can trigger strong responses in plants.

### 1.3. Atmospheric factors and their effect on irradiance

Diurnal, seasonal and latitudinal variation in spectral irradiance at ground level depend on solar elevation angle (affecting path length), on the composition of the traversed air mass (stratospheric ozone column, atmospheric water-vapour column, aerosols and clouds), and to a lesser extent on spectral reflectance from the ground surface (Gates, 1966; Górski, 1980; Johnson et al., 1967; Lee and Downum, 1991). Within the UV region, shorter wavelengths generally penetrate cloud more effectively than longer wavelengths, and this wavelength-dependency stems from multiple scattering between the cloud top and the atmosphere above, and radiance distribution at the cloud top which is further affected by solar elevation angle (Kylling et al., 1997; Lindfors and Arola, 2008; Seckmeyer et al., 1996). Water vapour in the atmosphere absorbs in the FR (alpha-band absorption) (Gates, 1966), and "Chappuis-band" absorption by the ozone layer reduces the transmittance of R during twilight (Hulburt, 1953).

Górski (1980, 1976) evaluated the extent of absorptance by the water vapour and ozone columns through irradiance measurements with a scanning spectroradiometer over three years, making at least four measurements every month in Puławy, Poland (51°N, 22°E). The R:FR photon ratio (645-665 nm and 715-735 nm bands) was lowest during spring, and high in late summer and autumn (presented as the inverse, FR:R photon ratio, in the study). These patterns were consistent with seasonal trends in absorptance of FR by water vapour and absorptance of R by the ozone column. A similar association between the R:FR photon ratio (658-662 nm and 728-732 nm bands) and atmospheric water-vapour content was presented in the studies by Lee and Downum (1991) and Goldberg and Klein (1977) mentioned above, i.e. that high R:FR photon ratios were recorded under conditions with high atmospheric water vapour.

### 1.4. Technological and methodological considerations

The vast majority of studies examining climatological changes in spectral irradiance report only a few days of data and there are no publications of continuous measurements at hourly or shorter intervals. This limitation is largely due to the measurement devices used in the past which made the collection of such measurements technically unfeasible or expensive. Scanning spectroradiometers can give precise spectral irradiance but require several minutes to scan across the entire spectrum from 400 nm to 800 nm, so cannot record near-instantaneous spectra. Although a correction can be applied based on a concurrent measurement of irradiance with a pyranometer, such a correction does not account for changes in the shape of the spectrum. This makes it very difficult to measure rapid changes in photon ratios such as those at twilight using such an approach. In addition, if the R:FR ratio is estimated from measurements using filtered pyranometers with broad wavebands of 600-700 nm and 700-800 nm, as done by e.g. Goldberg and Klein (1977), the ratios reported are difficult to compare with R:FR ratios, acquired later or computed, using narrower wavebands. The use of different bandwidths to calculate the R:FR ratios, or broadband sensors of different characteristics to directly measure the R:FR ratio, not only affects the estimated values but could also significantly affect the observed responses to various atmospheric conditions. While these issues can make studies difficult to compare, R:FR energy and photon ratios can at least be easily interconverted. The conversion factor from energy to photon ratios for bands centred at 660 nm and 730 nm respectively is *c.* 0.9; making a R:FR energy ratio of 1.28 equivalent to a R:FR photon ratio of 1.15.

Modern array spectrometers are capable of making the fast consecutive measurements needed to account for the high variability of solar radiation over time (Aphalo et al., 2016; Seckmeyer et al., 2008). Even so, ongoing and long-term spectral measurements over a biologically interesting wavelength range are scarce (Blumthaler et al., 2013; Ylianttila et al., 2005). Post processing of the data is not

**Table 1**
Studies reporting measurements and calculations of R:FR and B:R photon ratios during different seasons and different times of day.

| Location | Measurement period | Measurement device | Photon ratio definition | Direction of change in the photon ratio | Reference |
|---|---|---|---|---|---|
| Barrow, Alaska, USA (71°N 157°W); Rockwille, Maryland, USA (39°N, 77°W); Pacific end of the Panama Canal (9°N 80°W) | Clear days during one year | Filtered pyranometers | 600-700 nm and 700-800 nm (R:FR)* | Differences in the daytime R:FR ratio* owing to water vapour absorption. At sunrise the ratio was generally lower than at midday. Exact elevations not given, but described as "various solar zenith distances". | Goldberg and Klein (1977) |
| Tromsø, Norway (69°N 18°E); Longyearbyen, Svalbard (78°N 15°E) | March-October (Tromsø); 24-25 June and 19-21 August (Longyearbyen) | Pyranometer | Bandwidth of 25 nm centred on 660 nm and 730 nm (R:FR) | R:FR ratio varying between *c* 0.7 and 1.1. Ratios under 0.9 were recorded when the solar elevation angle was $< 4°$. Lowest R:FR photon ratios of the day were recorded at low solar elevation angles between *c* 4° to -2°. | Nilsen (1985) |
| Logan, Utah, USA (42°N, 112°W) | Mid-summer | Scanning spectroradiometer | 660 nm / 730 nm (R:FR) | Declining R:FR ratio at solar elevation angles range $-10° < \alpha \leq 5°$ compared to daytime values. | Salisbury (1981) |
| Loughborough, UK (52.8°N 1°W) | 19 different occasions over four years covering all months except February and March | Scanning spectroradiometer | 655-665 nm and 725-735 nm (R:FR) | R:FR ratio was *c* 1.15 for solar elevation angle $> 7.5°$. For solar elevation angle $< 7.5°$, the ratio tended to drop, but showing high variability ranging from 0.5 to 1.5 at solar elevation angles between *c* 0° to 10°. | Hughes et al., (1984) |
| | | | 410-500 nm and 610-700 nm (B:R) | B:R ratio *c* 0.87 during the daytime, increasing up to *c* 3.0 at solar elevation angles between *c* 0° to -10°. | |
| Miami, USA (25°N, 80°W) | 2-8 January and 18 June-4 July | Scanning spectroradiometer | 600-700 nm and 725-735 nm (R:FR) | Lowest value for R:FR ratio *c* 0.75 before sunrise, increasing up to *c* 2.0 after sunrise, varying during daytime from 1.21 to 1.48. | Lee and Downum (1991) |
| | | | 400-500 nm and 600-700 nm (B:R) | B:R ratio *c* 0.75 during the daytime, increasing up to *c* 1.5 around sunrise/sunset. | |
| Kilpisjärvi, Finland (69°N 20°E) | 17-20 June | Not specified | Not specified | R:FR ratio declining from 1.2 at mid-day to 0.5 at midnight. B:R increasing from 0.85 at mid-day to 1.3 at midnight. | Taulavuori et al., (2010) |
| Basel, Switzerland (47 °N 7° E) | One year | Array spectrometer | 655-665 nm and 725-735 nm (R:FR) | Lowest value for R:FR ratio *c* 0.8 at <10°, increasing up to *c* 1.2 >10°. | Chiang et al., (2019) |

* Energy ratio given.

straightforward, especially in the UV range where the spectral structure of the dark signal and stray light generate noise and potential errors that require specific protocols to correct (Aphalo, 2017; Aphalo et al., 2016). As a consequence, array spectrometers usually lack the precision of scanning spectroradiometers, particularly at short wavelengths (reviewed by Bais et al., 2018). The collection and analysis of continuous measurements are also now easier because of improvements in computing power and more-accessible computer software allowing greater capacity for the recording and storage of data, and its subsequent processing.

Radiative transfer modelling, which relies on our understanding of the processes affecting the transmission of radiation through the atmosphere and our capacity to model these processes, also provides us with an opportunity to test how atmospheric factors affect the quantity and quality of solar radiation incident at the Earth's surface and available to plants (Brelsford, 2016). However, model validation has mostly been done for cloudless skies. Furthermore, validation with clouds have used 1D models, that make non-physical representations of clouds. This in turn results in a mismatch between modelled and measured data (Fauchez et al., 2018). The 3D structures of clouds are difficult to represent in models due to variation in their shape and number, and their 3D radiative effects are also wavelength dependent (Okata et al., 2017). Thus, attempts to apply cloud radiative forcing to climate models have given inconsistent results due to radiative transfer model-dependency (IPCC, 2014).

### 1.5. Aim and scope of the current study

As explained above, it is important to improve our understanding of geographical, temporal, and weather-related patterns in spectral photon ratios important to plants. With this objective, we acquired continuous time-series of spectral irradiance at one-minute intervals over 15 months at a low latitude location (Gual Pahari, India) and over 6 months at a high latitude location (Helsinki, Finland). At each location, matching data on atmospheric water-vapour content, total ozone and aerosol optical depth (AOD) were also collected. Our aim was to use these data to assess whether different spectral patterns are mainly driven by the differences in solar elevation angle at different latitudes and times of the year, and/or by short-term and seasonal variation in atmospheric factors. In addition to measurements with array spectrometers, we simulated the spectral irradiance at ground level for the same locations with *libRadtran* (a library of radiative transfer routines and programs) using observed and modified values for each of the atmospheric parameters considered (Emde et al., 2016). We used these radiative transfer simulations to check for artefacts in measurements of spectral irradiance and to infill gaps in the measured data, as well as to identify which atmospheric factors might underlie observed patterns in spectral quality. This approach has previously been successfully employed for estimating daily biologically-effective UV doses in outdoor experiments (Kotilainen et al., 2008; Morales et al., 2013, 2010) and for assessing enhancement errors in UV-B supplementation with lamps simulating the effects of ozone depletion (Kotilainen et al., 2011). Comparing simulated irradiances with measured spectra enables more accurate interpretation of the possible shortcomings and discrepancies in existing datasets resulting from technical and methodological issues and improves our capability to assess the quality of recorded data.

Based on known responses of plants to the spectral quality of light, we explore the possible roles of the observed changes in spectral photon ratios as sources of information for plant acclimation, and identify gaps worthy of further study in relation to the role of sunlight-driven photomorphogenesis in the ecology of plants.

## 2. Materials and Methods

### 2.1. Irradiance measurements

Solar spectra were recorded in Helsinki, Finland (60.20°N, 24.96°E, 27 m asl) between March and September 2017 and in Gual Pahari, India (28.43°N, 77.14°E, 257 m asl) between September 2016 and November 2017. Helsinki is a high-latitude location in northern Europe, while Gual Pahari in the northern part of India (close to New Delhi) is in the subtropical region. The two locations differ strongly from each other in terms of their climate. The annual average temperature, for example, is *c* 5°C in Helsinki and *c* 25°C in Gual Pahari, while other factors such as solar radiation, water vapour column, and total ozone column also differs between these two locations (see, e.g., Kållberg et al., 2005).

An array spectrometer was installed at each location, enclosed in a thermally stabilised box and connected through a 10 m-long optical fibre to a cosine diffuser. The spectrometers had been calibrated for measurements of solar radiation between 340-900 nm (Flame-S, Ocean Optics, Dunedin, FL, USA). The calibration was done with lamps traceable to the National Institute of Standards and Technology (NIST), in Ocean Optics' laboratory meeting ISO9001 requirements. The calibration was done for the instrument as a complete setup, with the diffuser in place, connected to the instrument with an optical fibre (specific for each diffuser). Thus, possible spectral features of the diffuser and of the whole measurement system are accounted for by the calibration. In Helsinki, the instrument was deployed on the rooftop of the Finnish Meteorological Institute with an essentially unobscured horizon. In Gual Pahari, the instrument was deployed on the rooftop of a building belonging to The Energy and Resources Institute's (TERI) research and development centre. While the horizon was largely unobscured over a broad sector to the South, from East to West, nearby trees partially obstructed the view to the North. Both instruments were regularly cleaned and checked to ensure that they were well aligned. A Kipp & Zonen CM11 pyranometer, at the Helsinki site, co-located with the Flame spectrometer, was used to corroborate the Flame measurements.

The diffuser (model UV-J1002-SMA by Schreder) only has a small cosine error; according to data provided by the manufacturer, the error is smaller than 2.5% for incident zenith angles $<70°$, data corroborated by Kärhä et al. (2014). To explore whether the non-ideal cosine response would affect the accuracy of our results, we evaluated its potential effect on spectral photon ratios at small solar elevation angles (-5° to 20°; SI Fig. 1). Essentially, this analysis showed that the cosine error of the diffuser, while larger, did not introduce significant biases to our findings at these low solar elevation angles.

Light spectra were acquired every minute and stored as raw detector counts plus metadata using the R-interface to the Java driver from Ocean Optics (R package rOmniDrive, and the OmniDriver runtime) called from an R script. Using a predefined discrete set of integration times between 0.0025 and 0.6 seconds, the integration time was dynamically adjusted to generally reach a number of counts corresponding to around 60-70% of the instrument's saturation level. The script included a protocol for true dark measurements at night time that was used to correct the baseline irradiance (Aphalo et al., 2016, 2012). Post-processing was done in R version 3.5.0 (R Core Team, 2017), using functions from package ooacquire (Aphalo, 2015). Calibration data supplied by Ocean Optics were imported into R. Processing steps were: 1) linearization, 2) conversion of raw detector counts to counts per second, 3) subtraction of the dark signal, 4) convolution with a vector of pixel calibration constants to obtain a spectrum expressed as spectral photon irradiance (mol $m^{-2}$ $s^{-1}$ $nm^{-1}$). Data presented are confined to periods when irradiance of photosynthetically active radiation (PAR) > 1 μmol $m^{-2}$ $s^{-1}$. This restriction was imposed to exclude any potentially unreliable data at very low irradiances approaching the limit of sensitivity of the spectrometer. This resulted in total 188 525 spectra processed for Helsinki, Finland and 238 136 spectra for Gual Pahari, India.

### 2.2. Irradiance simulations

Incident solar spectral irradiance (290-900 nm) at the two locations

was simulated with the *uvspec* model from libRadtran, version 2.0.1, radiative transfer package (Emde et al., 2016). The *uvspec* model calculates the radiation field in the Earth's atmosphere. See Mayer and Kylling (2005) and Emde et al. (2016) and references therein for studies comparing and validating uvspec/libRadtran against other models and surface, balloon and aircraft measurements of UV and visible radiation. The constituents of the atmosphere, including various trace gases and aerosols, are model inputs. The absorption and scattering properties of these constituents are taken from the algorithms and databases provided with libRadtran. The extraterrestrial spectrum above the atmosphere and the reflecting surface at the bottom are the boundary conditions. Simulations of irradiance at 15 min intervals were calculated for solar elevation angles $> 5^{\circ}$, whereas those $< 5^{\circ}$ were calculated at 5 min intervals (Lindfors et al., 2009). The parameters adjusted in the model were cloud optical depth, total ozone column, column-integrated water vapour, and surface type (according to the International Geosphere Biosphere Programme (IGBP, 1992)). Cloud optical depth of ten was chosen to represent average conditions (Chang and Li, 2005; Serrano et al., 2014). The spectral albedo of the ground was determined as a function of solar elevation angle based on the surface type. We used the DISORT radiative transfer solver (Stamnes et al., 1988) for daytime irradiance, but for solar elevations $< 20^{\circ}$ pseudospherical geometry was included to account for the curvature of the Earth (SDISORT; Dahlback and Stamnes, 1991).

### 2.3. Atmospheric data

Water vapour and aerosol optical depth (AOD) input data were retrieved from AERONET (Aerosol Robotic Network), providing continuous cloud-screened observations of the water-vapour column and AOD based on measurements using a Cimel sun photometer (online resource: http://aeronet.gsfc.nasa.gov, data were downloaded on 5 March 2018). Total ozone column input data were obtained from measurements by the Ozone Monitoring Instrument (OMI) on board NASA's EOS Aura satellite (OMUVB Collection 3, PGE v1.3; for an ascending orbit only with SZA $< 88$, online resource: https://avdc.gsfc.nasa.gov/pub/data/satellite/Aura/OMI/V03/L2OVP/OMUVB/, data were downloaded on 5 March 2018).

### 2.4. Data analysis

All computations and statistical analyses regarding photon irradiances and spectral photon ratios and their correlations with atmospheric factors were done in R version 3.5.0 (R Core Team, 2017). Photon irradiances and photon ratios were calculated as follows from spectral photon irradiance using functions from the R for photobiology packages (Aphalo, 2015): blue:green (B:G) ratio calculated from photon irradiance for the bands 420-490 nm and 500-570 nm, blue:red (B:R) ratio for the bands 420-490 nm and 620-680 nm, red:far-red (R:FR) ratio for the bands 655-665 nm and 725-735 nm. Blue, green and red according to Sellaro et al. (2010), and R:FR according to Smith (1982). The response of a R and FR sensor (SKR110, Skye Instruments, Powys, UK) was simulated by convolution of spectral irradiance by the spectral response function of the two channels of the sensor as published by the manufacturer (from R package photobiologySensors) and integrated over these wavelengths. To ensure the validity of the simulation, a calibration was also done *in silico* against spectral irradiance data for sunlight on 22 June 2010, near solar noon in Helsinki, under partly cloudy conditions (sun.spct from R package photobiology). Photon irradiance of PAR (400-700 nm) was calculated as a reference, to assess whether variation patterns of spectral photon ratios were different from those of PAR over the range of solar elevation angles. Spectral irradiances and spectral photon ratios were plotted using the ggplot2 (Wickham, 2016) and ggridges (Wilke, 2018) packages for visualizing changes over time. This approach was used to smooth out daily fluctuations and highlight longer-term patterns in the data set. We used three different ranges of solar elevation angles, $< 0^{\circ}$ ($\alpha \leq 0^{\circ}$), between $0^{\circ}$ and $20^{\circ}$ ($0^{\circ} < \alpha \leq 20^{\circ}$), and above $20^{\circ}$ ($20^{\circ} < \alpha \leq 90$) in order to highlight the diurnal patterns in spectral photon ratios. This approach was used to account for the length of the path of sunlight through the atmosphere and to separate the solar elevation angle effect from the changes in atmospheric factors.

The contribution of each factor: total ozone, water-vapour column and aerosol optical depth to the variations in the spectral irradiances and spectral photon ratios, taking into account the effect of solar elevation angle, were quantified using a multiple regression model, with 95 % bootstrap confidence intervals. This was done using the relaimpo package (Groemping, 2006). The “averaged over ordering method” with metric “lmg” (Lindeman et al., 1980) was used, as this metric represents the variance explained by each variable, independent of the order of the predictors in the model. Here, we used the same solar elevation angle ranges as with the spectral photon ratios data.

## 3. Results

We start by summarizing patterns of change in the spectral photon ratios of interest over the entire measurement period at our two locations and three ranges of solar elevation angle throughout the year. Secondly, we exemplify the effect of solar elevation angle, water vapour column and cloudiness on diurnal patterns of photon ratios and PAR-irradiance through example days. In the third part, we quantify the contribution of atmospheric factors and the effect of solar elevation angle to the variation in the photon ratios through a multiple regression model.

### 3.1. Diurnal changes in spectral photon ratios across seasons

In Helsinki, Finland, the B:G photon ratio was bigger at $\alpha \leq 0^{\circ}$ (averages up to 1.41 in March and April) than at higher solar elevations (averages between 0.87-0.98: Fig. 1A, Table 2). This ratio showed a similar pattern throughout the measurement period, but the B:G photon ratio, measured when the sun was below the horizon, was higher during March-May compared with the rest of the year (Fig. 1A, Table 2). The largest values of the B:R photon ratio (average up to 1.72 in April) occurred at $\alpha \leq 0^{\circ}$, not at $0^{\circ} < \alpha \leq 20^{\circ}$ nor other higher solar elevation angles (typically B:R *c* 1.0), and as with the B:G photon ratio there was no clear seasonal pattern (Fig. 1B, Table 2). The R:FR photon ratio was consistently smallest when the sun was below the horizon ($\alpha \leq 0^{\circ}$, average 0.89 in March: Fig. 1C, Table 2). However, the ratio was largest at $0^{\circ} < \alpha \leq 20^{\circ}$ (average up to *c* 1.35 in July) compared with the other solar elevations examined during June-August. At $\alpha > 20^{\circ}$ the R:FR photon ratio was largest during June-September (average up to *c* 1.28 in August: Fig. 1C, Table 2).

In Gual Pahari, India, the values of the B:G photon ratio were similar to those in Helsinki and followed a similar diurnal pattern throughout the measurement period, but there was a larger spread of high values (c up to 1.8) measured at $\alpha \leq 0^{\circ}$ during June-August compared with the rest of the year (Fig. 2A, Table 2). The diurnal pattern in the B:R photon ratio produced larger and more variable values at $\alpha \leq 0^{\circ}$ during January-May, and even more so during June-September (up to *c* 3.2), whereas diurnal variation was small during October-December (Fig. 2B, Table 2). At $20^{\circ} < \alpha \leq 90^{\circ}$, the B:R photon ratio remained stable in Gual Pahari, at similar values to Helsinki, throughout the year, though with a slight tendency towards larger values during July and August. Again similarly, the R:FR photon ratio was consistently smallest when the sun was below the horizon at both locations (Fig. 1C & Fig. 2C) and the maximum R:FR values were attained at $0^{\circ} < \alpha \leq 20^{\circ}$ (highest average 1.55 in July, Fig. 2C, Table 2).

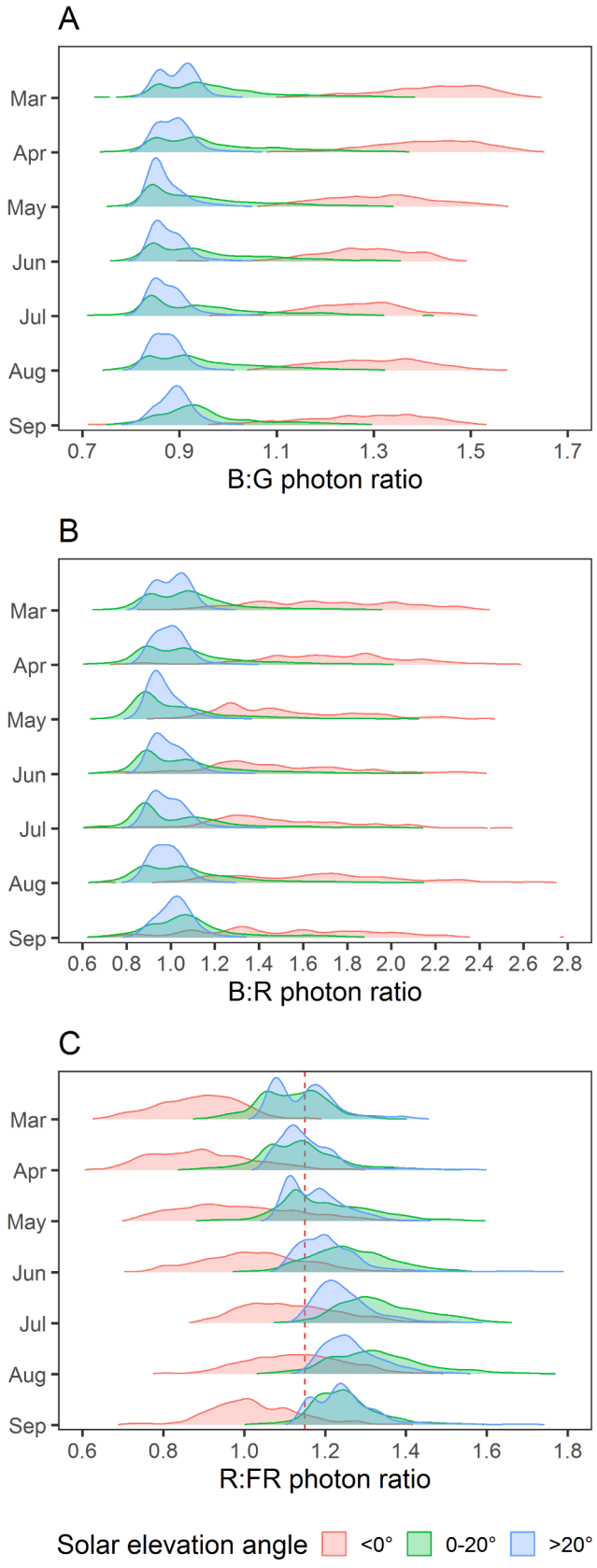


**Fig. 1.** A-C. Spectral photon ratios calculated from irradiance spectra measured in Helsinki, Finland. Solar elevation angles were divided into three sections to illustrate diurnal changes during each month: below the horizon (red), above the horizon but under 20 degrees (green) and above 20 degrees, i.e. the rest of the day (blue). The plots show the empirical distribution of calculated photon ratios for each month over the range of solar elevation angles. The figure summarizes 188 525 spectra recorded at one-minute intervals. Trailing tails were cut off with an aesthetic set for a one percent cut-off relative to the highest point of the density curves. A dashed red line in panel C at x = 1.15 indicates a typical daytime R:FR value commonly used as standard in the scientific literature.

### *3.2. The effect of solar elevation angle, atmospheric water vapour and cloudiness on spectral photon ratios*

Spectral photon ratios, calculated from the measured irradiances, depended on differences in atmospheric water vapour content and clouds together with the solar elevation angle at different times of day irrespective of whether they occur at “dusk” or “dawn”. To exemplify the effect of solar elevation angle, water vapour column and cloudiness on diurnal patterns in photon ratios and PAR-irradiance, two example days with contrasting atmospheric water vapour were plotted (Fig. 3 and Fig. 4). Water vapour in the atmosphere in general changes more across seasons than between individual dates during a certain month (SI Fig. 2A-B).

The effects of solar elevation angle and water vapour column on the spectral photon irradiance and spectral photon ratios under similar conditions to those measured were tested using simulated irradiances. Concerning all the photon ratios, the effect of cloudiness could be distinguished from that of atmospheric water vapour with the simulated irradiances, i.e. their effects on photon ratios were not equivalent. For Helsinki, Finland, these results are given in Fig. 5A, C, E and SI Fig. 3 and for Gual Pahari, India in Fig. 5B, D, F and SI Fig. 4.

In Helsinki, clouds and broken clouds, i.e. when a cloud was blocking the sun but not the sky, resulted in more diffuse radiation compared with direct radiation. This caused a higher proportion of blue, which is visible in the increased B:G and B:R ratios (compare Fig. 3A, B and Fig. 3C, D and Fig. 5A, C). The R:FR photon ratio remained relatively constant at $\alpha > 10^{\circ}$, but was higher in general when the atmospheric water vapour was higher (Fig. 3E, F, Fig. 5E). On days with lower atmospheric water vapour, the R:FR photon ratio started to increase when the sun got close to and above the horizon in the morning and correspondingly decreased in the evening towards sunset (Fig. 3E, Fig. 5E). Interestingly, this pattern changed on days when atmospheric water vapour was high, in that the R:FR photon ratio started to increase at *c* $\alpha < 15^{\circ}$ but then decreased as before when the sun got close to the horizon (Fig. 3F, Fig. 5E). In addition, the R:FR photon ratio showed similar variability due to clouds as the B:G and B:R photon ratios, but to a lesser extent. In comparison with the spectral photon ratios, PAR-irradiance did not follow any specific pattern during sunrise or sunset (Fig. 3G, H).

In Gual Pahari, similar to Helsinki, clouds and broken clouds resulted in more diffuse radiation compared with direct radiation and increased B:G and B:R ratios (compare Fig. 4A, B and Fig. 4C, D and Fig. 5B, D). The R:FR photon ratio in Gual Pahari, on days with a water vapour column that was lower than or similar to Helsinki, remained comparable during the day and declined after the sun dropped below horizon, but the ratio did not reach such low values as in Helsinki (compare Fig. 3E & Fig. 4E, Fig. 5E & Fig. 5F, Table 2). In cloudier evening conditions with higher atmospheric water vapour, the R:FR photon ratio started to increase up to 2.0 at *c* $\alpha$ 20°, and subsequently did not decrease below 1.1 during the rest of the day and through twilight (Fig. 4F). PAR-irradiance is given as a reference, for comparison with the spectral photon ratios during sunrise and sunset (Fig. 4G, H).

**Table 2**
Monthly averages (SE in parenthesis) of spectral photon ratios calculated from spectral irradiances measured in Helsinki, Finland, and Gual Pahari, India.

| Place | Ratio | Solar elevation angle range | Jan | Feb | Mar | Apr | May | Jun | Jul | Aug | Sep | Oct | Nov | Dec |
|---|---|---|---|---|---|---|---|---|---|---|---|---|---|---|
| HEL, FIN | B:G | $\alpha \leq 0^\circ$ | | | 1.41 (0.004) | 1.41 (0.003) | 1.31 (0.002) | 1.27 (0.002) | 1.26 (0.002) | 1.29 (0.003) | 1.27 (0.005) | | | |
| | | $0^\circ < \alpha \leq 20^\circ$ | | | 0.98 (0.001) | 0.97 (0.001) | 0.95 (0.001) | 0.96 (0.001) | 0.96 (0.001) | 0.95 (0.001) | 0.96 (0.001) | | | |
| | | $20^\circ < \alpha \leq 90^\circ$ | | | 0.90 (0.001) | 0.89 (0.001) | 0.87 (0.001) | 0.88 (0.001) | 0.88 (0.001) | 0.87 (0.001) | 0.89 (0.001) | | | |
| | B:R | $\alpha \leq 0^\circ$ | | | 1.70 (0.011) | 1.72 (0.009) | 1.53 (0.007) | 1.45 (0.007) | 1.50 (0.007) | 1.65 (0.001) | 1.49 (0.016) | | | |
| | | $0^\circ < \alpha \leq 20^\circ$ | | | 1.12 (0.003) | 1.10 (0.003) | 1.05 (0.003) | 1.10 (0.003) | 1.11 (0.003) | 1.10 (0.003) | 1.11 (0.003) | | | |
| | | $20^\circ < \alpha \leq 90^\circ$ | | | 1.01 (0.001) | 1.00 (0.001) | 0.98 (0.001) | 1.00 (0.001) | 1.00 (0.001) | 0.99 (0.001) | 1.02 (0.001) | | | |
| | R:FR | $\alpha \leq 0^\circ$ | | | 0.89 (0.003) | 0.90 (0.003) | 0.99 (0.003) | 1.03 (0.002) | 1.13 (0.002) | 1.13 (0.003) | 1.03 (0.004) | | | |
| | | $0^\circ < \alpha \leq 20^\circ$ | | | 1.12 (0.001) | 1.14 (0.001) | 1.20 (0.001) | 1.26 (0.001) | 1.35 (0.001) | 1.34 (0.001) | 1.27 (0.002) | | | |
| | | $20^\circ < \alpha \leq 90^\circ$ | | | 1.15 (0.001) | 1.16 (0.001) | 1.18 (0.001) | 1.23 (0.001) | 1.25 (0.001) | 1.28 (0.001) | 1.26 (0.001) | | | |
| GP, IND | B:G | $\alpha \leq 0^\circ$ | 1.15 (0.005) | 1.15 (0.005) | 1.17 (0.002) | 1.17 (0.003) | 1.21 (0.003) | 1.19 (0.007) | 1.28 (0.010) | 1.29 (0.010) | 1.10 (0.004) | 1.05 (0.002) | 1.03 (0.001) | 1.02 (0.001) |
| | | $0^\circ < \alpha \leq 20^\circ$ | 0.94 (0.002) | 0.95 (0.002) | 0.97 (0.002) | 0.94 (0.002) | 0.94 (0.002) | 0.96 (0.002) | 1.01 (0.002) | 0.98 (0.002) | 0.95 (0.001) | 0.92 (0.001) | 0.90 (0.001) | 0.92 (0.001) |
| | | $20^\circ < \alpha \leq 90^\circ$ | 0.84 (0.001) | 0.85 (0.001) | 0.86 (0.001) | 0.85 (0.001) | 0.85 (0.001) | 0.87 (0.001) | 0.89 (0.001) | 0.89 (0.001) | 0.85 (0.001) | 0.82 (0.001) | 0.81 (0.002) | 0.83 (0.001) |
| | B:R | $\alpha \leq 0^\circ$ | 1.32 (0.014) | 1.29 (0.015) | 1.36 (0.008) | 1.35 (0.009) | 1.46 (0.010) | 1.49 (0.020) | 1.66 (0.027) | 1.66 (0.029) | 1.25 (0.010) | 1.13 (0.006) | 1.05 (0.004) | 1.04 (0.006) |
| | | $0^\circ < \alpha \leq 20^\circ$ | 1.04 (0.003) | 1.08 (0.003) | 1.12 (0.003) | 1.03 (0.003) | 1.05 (0.004) | 1.11 (0.004) | 1.24 (0.005) | 1.17 (0.004) | 1.12 (0.002) | 1.04 (0.002) | 0.98 (0.002) | 1.01 (0.002) |
| | | $20^\circ < \alpha \leq 90^\circ$ | 0.90 (0.001) | 0.92 (0.001) | 0.93 (0.001) | 0.92 (0.001) | 0.92 (0.001) | 0.97 (0.001) | 1.03 (0.001) | 1.02 (0.001) | 0.93 (0.001) | 0.87 (0.001) | 0.84 (0.001) | 0.88 (0.001) |
| | R:FR | $\alpha \leq 0^\circ$ | 1.08 (0.004) | 1.06 (0.004) | 1.09 (0.004) | 1.08 (0.004) | 1.17 (0.004) | 1.28 (0.005) | 1.39 (0.006) | 1.38 (0.007) | 1.26 (0.003) | 1.10 (0.003) | 1.08 (0.002) | 1.10 (0.003) |
| | | $0^\circ < \alpha \leq 20^\circ$ | 1.16 (0.001) | 1.15 (0.001) | 1.20 (0.001) | 1.19 (0.001) | 1.29 (0.001) | 1.44 (0.002) | 1.55 (0.003) | 1.51 (0.002) | 1.43 (0.001) | 1.21 (0.001) | 1.14 (0.001) | 1.16 (0.001) |
| | | $20^\circ < \alpha \leq 90^\circ$ | 1.12 (0.001) | 1.10 (0.001) | 1.12 (0.001) | 1.14 (0.001) | 1.22 (0.001) | 1.31 (0.001) | 1.40 (0.001) | 1.40 (0.001) | 1.29 (0.001) | 1.14 (0.001) | 1.08 (0.001) | 1.09 (0.001) |




*(caption on next page)*

**Fig. 2.** A-C. Spectral photon ratios calculated from irradiance spectra measured in Gual Pahari, India. Solar elevation angles were divided into three sections to illustrate diurnal changes during each month: below the horizon (red), above horizon but under 20 degrees (green) and above 20 degrees, i.e. the rest of the day (blue). The plots show the empirical distribution of calculated photon ratios for each month over the range of solar elevation angles. The figure summarizes 238 136 spectra recorded at one-minute intervals. Trailing tails were cut off with an aesthetic set for a one percent cut-off relative to the highest point of the density curves. A dashed red line in panel C at x = 1.15 indicates a typical daytime R:FR value commonly used as standard in the scientific literature.

### 3.3. The effects of solar elevation angle, total ozone, water vapour column, and aerosol optical depth across different months

Total ozone column thickness was greatest during March-May in Helsinki, whereas in Gual Pahari ozone values were lower and remained more stable during the measurement period (after Brewer-Dobson circulation) (Fig. 6A). In both locations, atmospheric water vapour was highest during June-August, but it was generally higher in Gual Pahari than Helsinki throughout the monitoring period (Fig. 6B). Aerosol optical depth (AOD) measured at 500 nm remained more stable and lower in Helsinki than Gual Pahari (Fig. 6C).

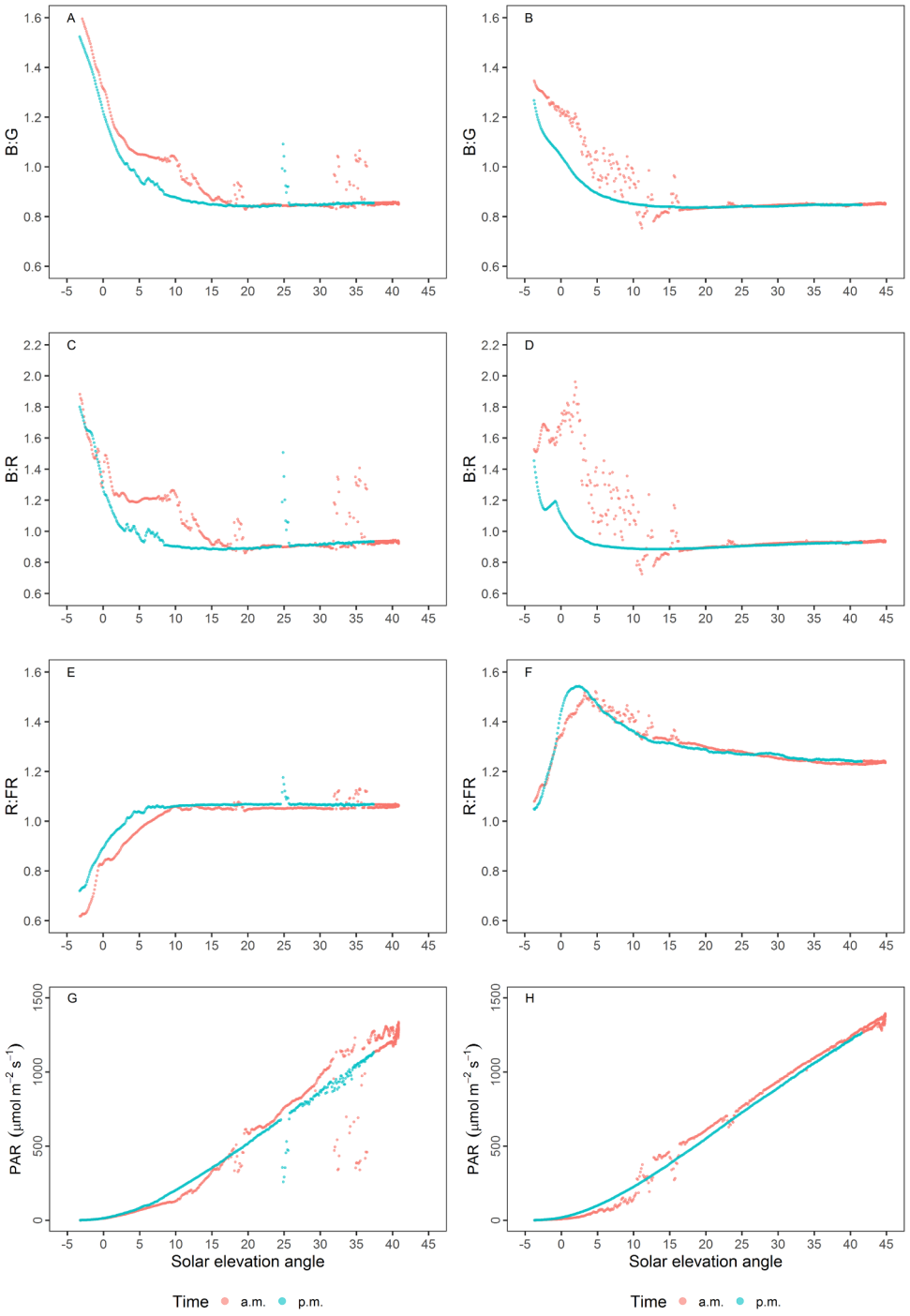


**Fig. 3.** A-H. Spectral photon ratios and PAR irradiance calculated from spectral irradiance measurements from Helsinki, Finland, plotted against solar elevation angle. The left-hand panels (A, C, E and G) present measurements from 18.04.2017, a relatively sunny day with scattered clouds during the day and with water vapour column average 0.36 cm (min 0.30 cm, max 0.41 cm) and total ozone 390 DU. The right-hand panels (B, D, F, H) are 11.08.2017, a day with relatively cloudy conditions before noon and with water vapour column average 2.0 cm (min 1.6 cm, max 2.4 cm) and total ozone 290 DU. Clouds obscuring the sun make a dip in the PAR irradiance graphs (G and H). Red circles are measurements before noon and blue circles after noon, recorded once per minute.

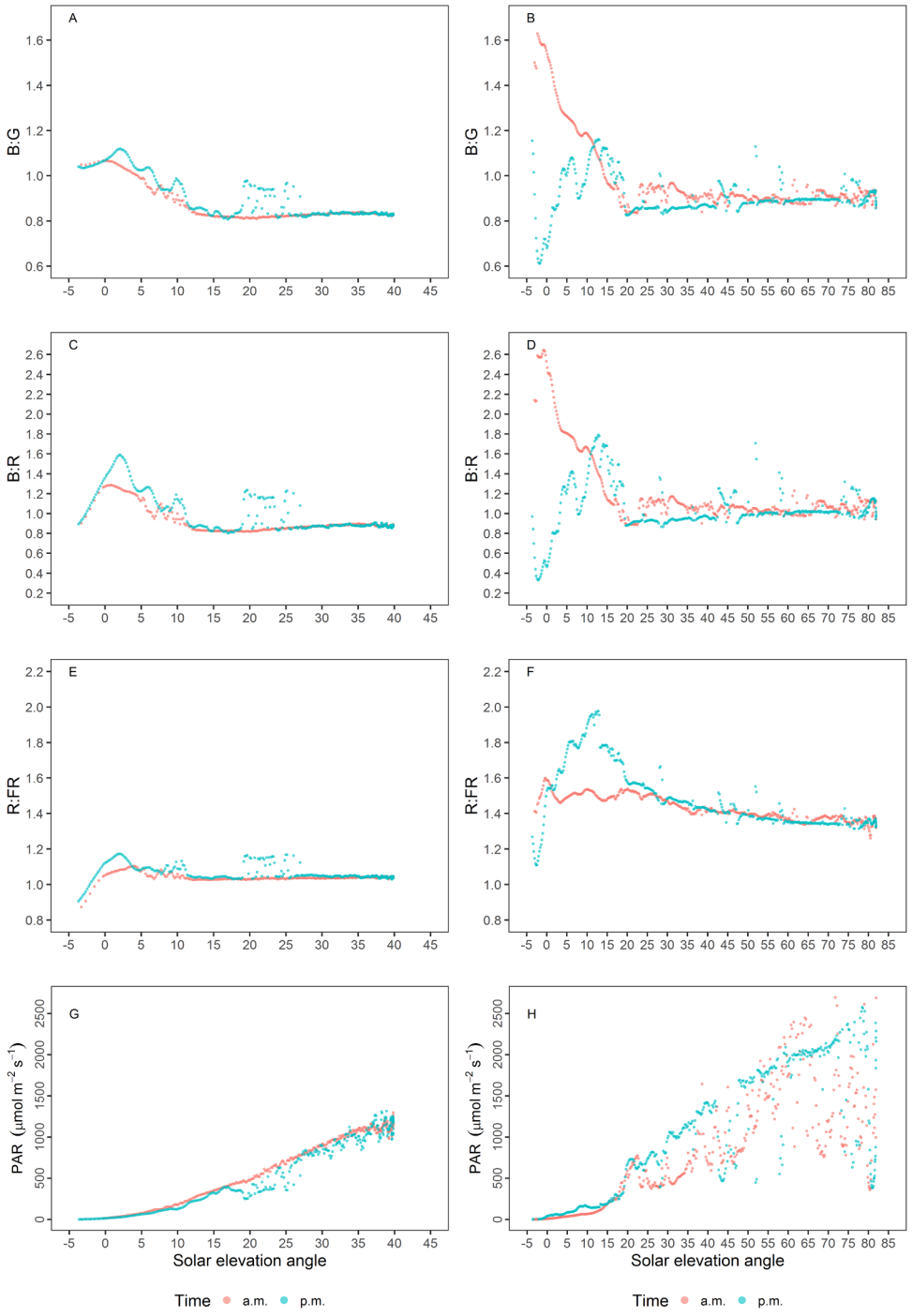


**Fig. 4.** A-H. Spectral photon ratios and PAR irradiance calculated from spectral irradiance measurements from Gual Pahari, India, plotted against solar elevation angle. The left-hand panels (A, C, E and G) present measurements from 11.1.2017, a relatively sunny and cloud-free day with water vapour column average 0.61 cm (min 0.50 cm, max 0.83 cm) and total ozone 260 DU. The right-hand panels (B, D, F, H) are 21.7.2017, a variably cloudy day with water vapour column average 5.9 cm (min 5.3 cm, max 6.9 cm) and total ozone 276 DU. Clouds obscuring the sun make a dip in the PAR irradiance graphs (G and H). Red circles are measurements before noon and blue circles after noon, recorded once per minute. Please note that the scales on the x-axis and y-axis are different from those in Fig. 3.

In order to quantify the contribution of total ozone, water vapour column, and AOD to the variation in the photon ratios and to separate the effect of solar elevation angle, the relative importance of these explanatory variables was assessed in a multiple regression model including all the calculated irradiances and spectral photon ratios (Table 3). The percentages presented in Table 3 give the size of the effect a specific factor had on the given spectral photon ratio. When the confidence interval does not include zero, then one can conclude that there is a statistically significant difference between the factors. This was the case for the majority of the comparisons made to estimate the relative contributions of the different factors (Table 3). In Helsinki, 18.2 % of variation in the B:G photon ratio was explained by solar elevation angle (lower elevation angle; larger ratio) at $\alpha \leq 0^{\circ}$ and 31.3 % at $0^{\circ} < \alpha \leq 20^{\circ}$. In addition, total ozone explained 10.6 % of the variation at $\alpha \leq 0^{\circ}$ (less total ozone, higher ratio). For the B:R photon ratio, solar elevation angle explained 12.1 % of the variation (lower elevation angle; larger ratio) at $0^{\circ} < \alpha \leq 20^{\circ}$. For the R:FR photon ratio, solar elevation angle, total ozone and atmospheric water vapour explained 30.1 %, 16.7 %, and 27.9 % of the variance, respectively, at $\alpha < 0^{\circ}$. The variance of the R:FR ratio was similar at higher elevations $0^{\circ} < \alpha \leq 20^{\circ}$ and at $20^{\circ} < \alpha \leq 90^{\circ}$: however, the contribution of atmospheric water vapour was higher (34.6 % and 34.5 %, respectively) and that of solar elevation angle was negligible. The R:FR photon ratio was smaller when there was more ozone and larger when there was more atmospheric water vapour. PAR-irradiance was only affected by solar elevation angle, explaining 67.6 %, 62.3 % and 24.0 % of the variance for the three solar elevation angle ranges, respectively. The contribution of AOD was negligible for all the photon ratios and PAR-irradiance.

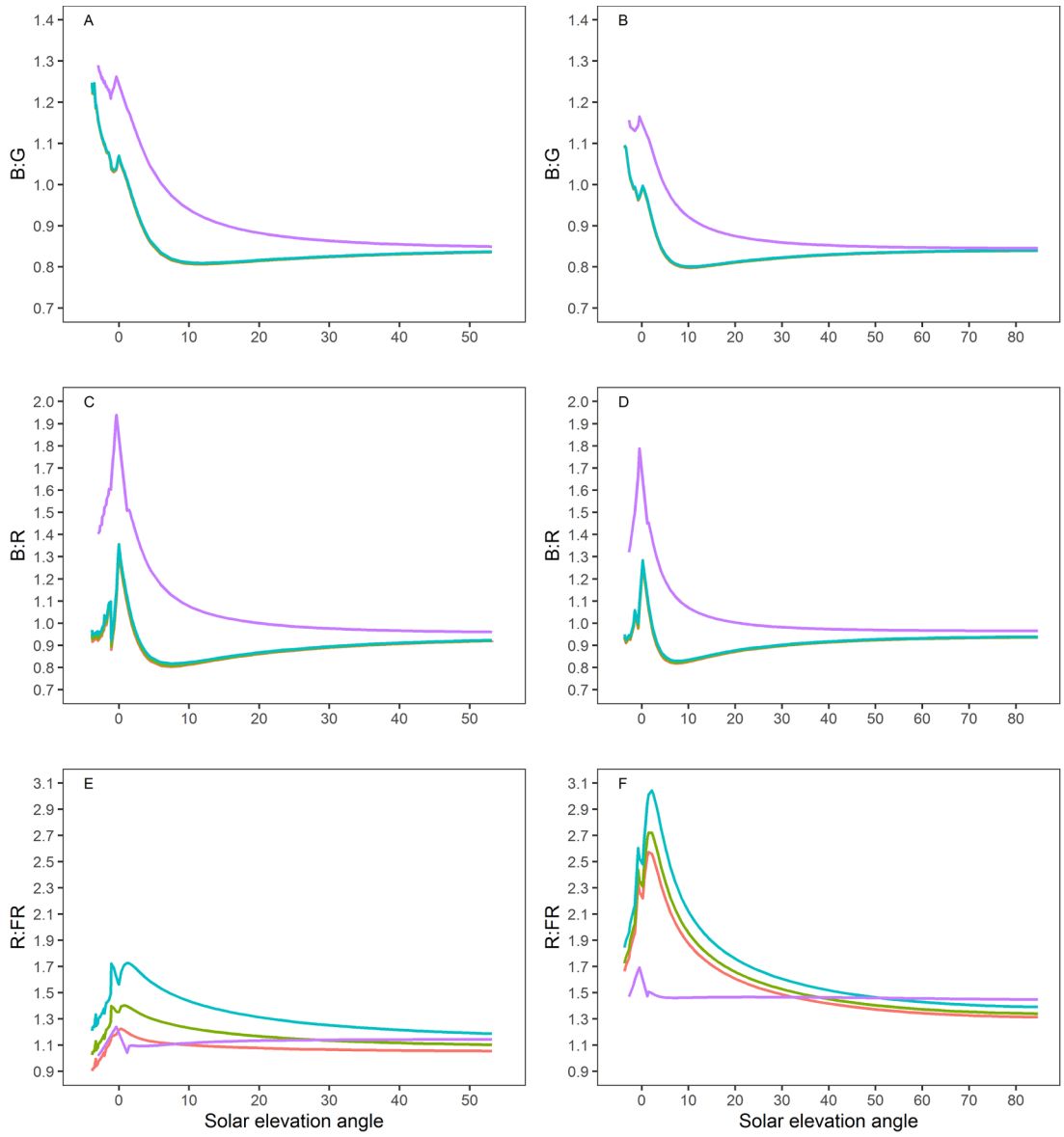


**Fig. 5.** A-F. The left-hand panels (A, C and E) present simulated irradiances for Helsinki, Finland, and the right-hand panels (B, D and F) present simulated irradiances for Gual Pahari, India. For both places on the date set for the simulation, 21st of June, demonstrating the effect of solar elevation angle and water vapour column at the three different levels and clouds; cloud optical thickness = 10. PAR irradiance is above 1 μmol $m^{-2}$ $s^{-1}$, hence similarly confined as the measurements. B:G photon ratio calculated 420-490 nm / 500-570 nm and B:R photon ratio calculated 420-490 nm / 620-680 nm, both according to Sellaro et al. (Sellaro et al., 2010); R:FR 655-675 nm / 725-735 nm according to Smith (Smith, 1982). For Helsinki (A, C and E) red line = water vapour column 0.5 cm; green line = water vapour column 1 cm; blue line = water vapour column 2 cm; purple line = water vapour column 2 cm with cloud optical thickness = 10. For Gual Pahari (B, D and F) red line = water vapour column 4.5 cm; green line = water vapour column 5 cm; blue line = water vapour column 6 cm; purple line = water vapour column 6 cm with cloud optical thickness = 10. The different water vapour columns with red, green and blue lines are so similar for B:G and B:R photon ratio, that the red and green lines are obscured by the blue line.

In Gual Pahari, variation in the B:G photon ratio was governed by similar drivers to Helsinki at $0^\circ < \alpha \leq 20^\circ$. Solar elevation angle explained 48.1 % of the variation (lower elevation angle; larger B:G ratio), and no other factors had a significant effect. At $\alpha \leq 0^\circ$, the explanatory factors differed from those in Helsinki, as the solar elevation angle had a negligible effect, but similar to Helsinki, total ozone explained 10.6 % of the variation at $\alpha \leq 0^\circ$ (less total ozone, higher B:G ratio). Again, at $20^\circ < \alpha \leq 90^\circ$, the explanatory factors differed from those in Helsinki. High atmospheric water vapour resulted in a larger B:G photon ratio, explaining 19.6 % of the response variance, while AOD explained 11.3 % of the response variance (higher AOD; tendency for lower B:G ratio).

The variation in the B:R photon ratio was explained in a similar manner to the B:G photon ratio. At $0^\circ < \alpha \leq 20^\circ$, solar elevation angle explained 32.4 % of the variation (lower elevation angle; higher B:R ratio). At $20^\circ < \alpha \leq 90^\circ$, high atmospheric water vapour resulted in a higher B:R photon ratio, and this factor explained 23.8 % of the response variance. In addition, AOD explained 10.5 % of the response variance (higher AOD; tendency for lower B:R ratio). In contrast to Helsinki, total ozone did not explain variation in the R:FR ratio; whereas, like in Helsinki, at $\alpha \leq 0^\circ$ solar elevation angle explained 19.5 % of the R:FR ratio variation. Atmospheric water vapour had a large effect on the R:FR photon ratio (a thicker water vapour column; larger R:FR ratio), for all three ascending solar elevation ranges, explaining 54.4 %, 70.3 % and 80.7 % of the variance, respectively. Similarly to Helsinki, PAR-irradiance was affected by solar elevation angle, explaining 71.0 %, 76.8 % and 56.8 % of the variance for the three solar elevation ranges, respectively. In addition, at $20^\circ < \alpha \leq 90^\circ$, AOD explained 5.9 % of the variance in PAR (larger AOD; smaller PAR-irradiance) (Table 3).

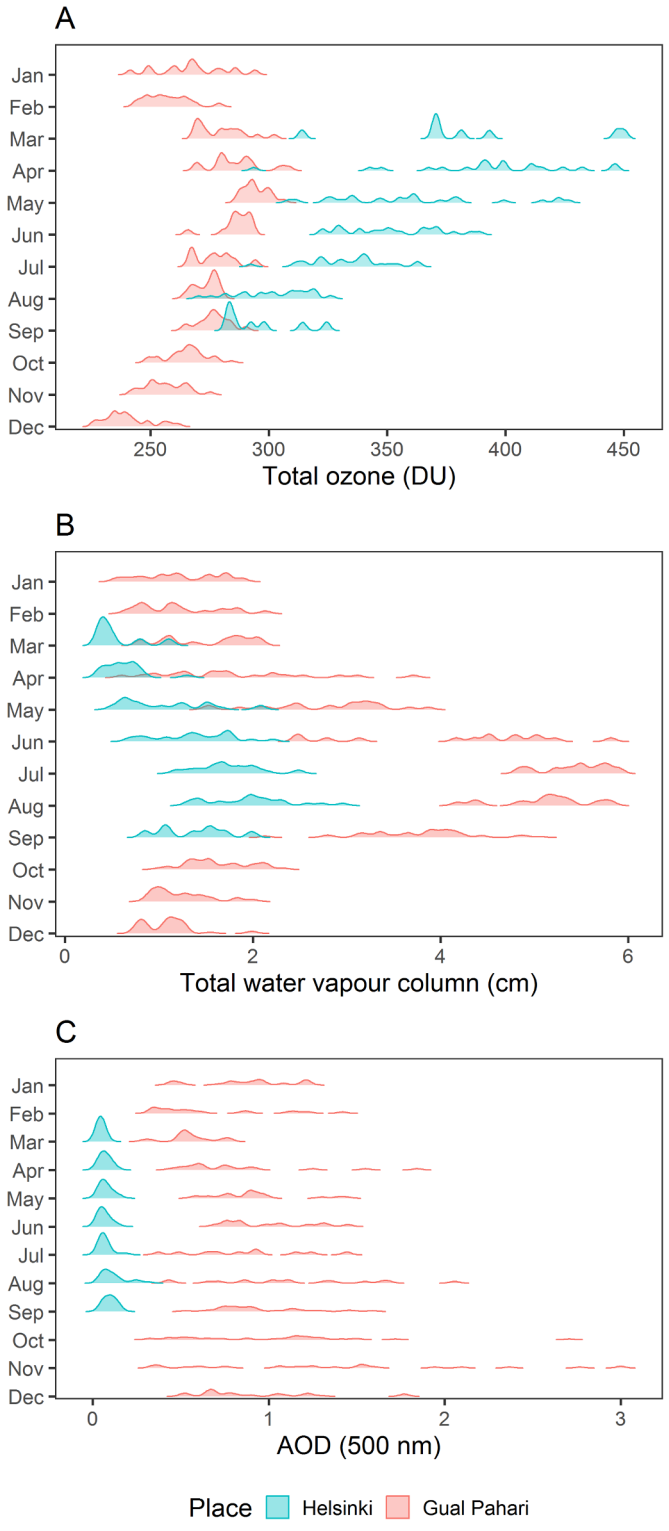


**Fig. 6.** A-C. Measured atmospheric properties; total ozone (A), total water vapour (B) and aerosol optical depth (C) for Helsinki, Finland and Gual Pahari, India, covering the same period as the spectral irradiance data, i.e. March – September 2017 for Helsinki, Finland and the whole year of 2017 for Gual Pahari, India. The plots show the empirical probability distribution of atmospheric properties recorded at different intervals for each month. Trailing tails were cut off with an aesthetic set for a one percent cut-off relative to the highest point of the density curves.

## 4. Discussion

In general, the diurnal and seasonal patterns in the spectral composition of sunlight at ground level were similar between the two locations we compared, Helsinki in Finland and Gual Pahari in India. Based on the analysis of over 400,000 recorded spectra, the B:G and B:R photon ratios followed diurnal patterns that were relatively consistent over time, whereas diurnal patterns in the R:FR photon ratio varied over the measurement period.

### *4.1. Diurnal and seasonal patterns in the B:G and B:R ratios*

Our analysis of the relative importance of solar elevation angle at different times of day in controlling spectral photon ratios showed that at $0^\circ < \alpha \leq 20^\circ$, the diurnal patterns in B:G and B:R photon ratios depended similarly on solar elevation angle at both locations (lower elevation angle; larger ratios). In contrast, the effect of the solar elevation angle on B:G ratio at $\alpha \leq 0^\circ$ was only apparent in Helsinki. For both locations, there was a small effect of total ozone on variation in the B:G ratio at $\alpha \leq 0^\circ$: less total ozone, led to a higher B:G ratio. The effect of the water vapour column on the B:G and B:R ratios (high atmospheric water vapour, higher photon ratios) was only apparent in Gual Pahari, where variance in the B:R photon ratio was also explained by the AOD at $20^\circ < \alpha \leq 90^\circ$.

These are the first detailed measurements published showing diurnal and seasonal patterns in the B:G and B:R ratios across different locations throughout the day. These patterns provide the context required to examine putative plant responses to blue light as an environmental cue, for instance; the potential role of blue light as a cue regulating spring phenology (Brelsford et al., 2019; Brelsford and Robson, 2018); a role for green light relative to red and blue light in modifying plant growth and development (Folta and Maruhnich, 2007); and of the B:G ratio in eliciting plant responses to shade (Sellaro et al., 2010).

Past studies based on periodic measurements at specific wavelengths proposed that the B:R photon ratio follows a diurnal pattern, being higher during twilight than during the rest of the day (Hughes et al., 1984; Johnson et al., 1967). The current study, partly corroborates this proposal, as our continuous measurements found the B:R photon ratio to increase when the sun was near or below horizon. However, it also fluctuated, presumably due to clouds, during the day when the sun was well above the horizon, producing large B:R values (up to *c* 1.6, that is close to the highest overall values occurring when the sun is close to horizon). Such generalisations do not exist in the literature for the B:G photon ratio, but we were able to confirm from our data that both the B:G and B:R ratios show similar response to atmospheric conditions.

### *4.2. Atmospheric water vapour and the R:FR ratio*

In accordance with previous research, our results show that the diurnal pattern in the R:FR photon ratio is closely linked to the amount of atmospheric water vapour (Górski, 1976; Lee and Downum, 1991), as the R:FR ratio varied with cloudiness and followed the seasonal pattern in the atmospheric water column thickness (Górski, 1980). This assertion was confirmed by measurements at both locations (Fig. 3E, F and Fig 4E, F) and from modelled spectral irradiances (Fig 5 and SI Fig. 3 and SI Fig. 4). This pattern was more pronounced at Gual Pahari, India where the water column thickness is larger than in Helsinki, Finland.

Published measurements of diurnal changes in the R:FR photon ratio in sunlight, have often shown decreases in R:FR when the sun was near or below horizon, compared with a higher and relatively stable R:FR ratio for the rest of the day (e.g Fig. 3E of this study and Holmes and Smith, 1977a; Nilsen, 1985). However this pattern is not consistently found across the literature, with substantial deviations

**Table 3**
The percentage of variance in irradiance explained by each explanatory variable in the multiple regression model ( ± 95% bootstrap CI in parentheses). Effects are presented for PAR irradiance and three major spectral photon ratios important in plant photobiology across three sets of solar elevation angles, consistent with Table 2. Significant pairwise comparisons between different factors are marked with *. Spectral photon ratios were calculated from spectral irradiances measured in Helsinki, Finland, and Gual Pahari, India. The contribution of an individual regressor less than one percent is marked as <1.0. The values do not add up to 100 %, as additional factors, e.g, cloudiness, are not included in the analysis as AERONET instruments require cloud-free conditions (sun and sky area close to sun) to measure the water vapour column and the aerosol optical depth (AOD). Thus, days with completely cloudy conditions are not included in this analysis.

| Place | Ratio/ irradiance | Solar elevation angle range | Solar elevation angle % (A) | Total ozone % (B) | Total water vapour column % (C) | AOD (500 nm) % (D) | A-B | A-C | A-D | B-C | B-D | C-D |
|---|---|---|---|---|---|---|---|---|---|---|---|---|
| HEL, FIN | B:G | $\alpha \leq 0^\circ$ | 18.2 (17.0-19.3) | 10.6 (9.6-11.6) | 6.8 (6.1-7.6) | 2.2 (1.7-2.8) | * | * | * | * | * | * |
| | | $0^\circ < \alpha \leq 20^\circ$ | 31.3 (30.7-32.0) | <1.0 | <1.0 | <1.0 | * | * | * | * | * | NS |
| | | $20^\circ < \alpha \leq 90^\circ$ | <1.0 | 1.7 (1.5-1.8) | <1.0 | <1.0 | * | * | NS | * | * | * |
| | B:R | $\alpha \leq 0^\circ$ | <1.0 | 2.3 (1.8-2.9) | <1.0 | 2.3 (1.7-3.1) | * | * | * | * | NS | * |
| | | $0^\circ < \alpha \leq 20^\circ$ | 12.1 (11.6-12.7) | <1.0 | <1.0 | <1.0 | * | * | * | * | * | * |
| | | $20^\circ < \alpha \leq 90^\circ$ | <1.0 | <1.0 | <1.0 | <1.0 | * | * | * | * | * | * |
| | R:FR | $\alpha \leq 0^\circ$ | 30.1 (29.1-31.1) | 16.7 (15.9-17.4) | 27.9 (27.0-28.7) | 2.0 (1.8-2.2) | * | * | * | * | * | * |
| | | $0^\circ < \alpha \leq 20^\circ$ | <1.0 | 18.3 (18.0-18.6) | 34.6 (34.0-35.2) | 2.6 (2.5-2.7) | * | * | * | * | * | * |
| | | $20^\circ < \alpha \leq 90^\circ$ | 1.4 (1.3-1.6) | 13.9 (13.6-14.2) | 34.5 (33.9-35.1) | 4.5 (4.3-4.6) | * | * | * | * | * | * |
| | PAR | $\alpha \leq 0^\circ$ | 67.6 (66.5-68.8) | <1.0 | <1.0 | <1.0 | * | * | * | * | * | * |
| | | $0^\circ < \alpha \leq 20^\circ$ | 62.3 (61.7-62.9) | <1.0 | <1.0 | 1.0 (0.92-1.1) | * | * | * | * | * | * |
| | | $20^\circ < \alpha \leq 90^\circ$ | 24.0 (23.5-24.6) | <1.0 | <1.0 | 1.3 (1.2-1.4) | * | * | * | * | * | * |
| GP, IND | B:G | $\alpha \leq 0^\circ$ | <1.0 | 10.6 (9.6-11.7) | 10.4 (8.7-12.1) | 2.1 (1.5-2.7) | * | * | * | NS | * | * |
| | | $0^\circ < \alpha \leq 20^\circ$ | 48.1 (47.4-48.9) | 1.3 (1.2-1.5) | 3.6 (3.3-3.8) | 3.2 (2.9-3.4) | * | * | * | * | * | NS |
| | | $20^\circ < \alpha \leq 90^\circ$ | 5.5 (5.3-5.7) | 3.0 (2.9-3.1) | 19.6 (19.2-20.0) | 11.3 (10.9-11.7) | * | * | * | * | * | * |
| | B:R | $\alpha \leq 0^\circ$ | 8.7 (7.7-9.7) | 5.8 (5.2-6.5) | 10.1 (8.5-11.8) | 1.4 (1.0-1.9) | * | NS | * | * | * | * |
| | | $0^\circ < \alpha \leq 20^\circ$ | 32.4 (31.8-33.2) | <1.0 NS | 5.6 (5.2-6.0) | 3.9 (3.6-4.2) | * | * | * | * | * | * |
| | | $20^\circ < \alpha \leq 90^\circ$ | 7.9 (7.6-8.1) | 2.1 (2.0-2.2) | 23.8 (23.4-24.2) | 10.5 (10.2-10.8) | * | * | * | * | * | * |
| | R:FR | $\alpha \leq 0^\circ$ | 19.5 (18.5-20.6) | 2.6 (2.4-2.8) | 54.4 (52.8-55.9) | <1.0 | * | * | * | * | * | * |
| | | $0^\circ < \alpha \leq 20^\circ$ | <1.0 | 5.2 (5.0-5.4) | 70.3 (69.8-70.8) | <1.0 | * | * | * | * | * | * |
| | | $20^\circ < \alpha \leq 90^\circ$ | 2.33 (2.28-2.38) | 4.9 (4.8-5.1) | 80.7 (80.3-81.1) | <1.0 | * | * | * | * | * | * |
| | PAR | $\alpha \leq 0^\circ$ | 71.0 (69.3-72.8) | <1.0 | <1.0 | 1.3 (1.0-1.6) | * | * | * | * | * | * |
| | | $0^\circ < \alpha \leq 20^\circ$ | 76.8 (76.3-77.2) | <1.0 | <1.0 | 2.8 (2.7-3.0) | * | * | * | * | * | * |
| | | $20^\circ < \alpha \leq 90^\circ$ | 56.8 (56.3-57.3) | 3.1 (3.0-3.2) | 1.65 (1.60-1.69) | 5.9 (5.8-6.1) | * | * | * | * | * | * |

sometimes reported (e.g. Hughes et al., 1984; Lee and Downum, 1991). One source of this discrepancy is the different conditions prevailing during the measurements, especially the aforementioned atmospheric water vapour content, that are not always taken into account. Another possible source of this discrepancy is the difference in spectral sensitivity of the different types of sensors used to measure photon ratios. The R:FR photon ratio is lower according to the "simulated Skye SKR-110 sensor" than when calculated from spectral irradiance, according to Smith's R:FR definition (Smith, 1982). This happens because Smith's definition assumes narrow spectral response bands with a rectangular shape, while most broadband sensors have bell shaped spectral response functions; in this particular case covering a broader range of wavelengths (SI Fig. 5A-H and SI Fig. 6A-B). Furthermore, SKR-110 sensor data may have small alignment errors between the channels, not simulated here, which can lead to additional errors at very low solar elevation angles, together with possible levelling errors due to field installation that deviates from the horizontal.

### *4.3. The R:FR ratio is a signal for shade but also carries information related to weather conditions and seasonal changes*

To understand the relevance for plant photobiology of the diurnal and seasonal patterns in spectral composition affecting R:FR ratio, the signals conveying information to plants need to be identified. Measurements done in Loughborough, UK (52.8°N, 1.2°W) attempted to identify whether the large drop (*c* 35 %) in the R:FR photon ratio during twilight has a signalling role in plants (Hughes et al., 1984). The decrease in R:FR corresponds to a decrease in the phytochrome photoequilibrium from 0.54 in full sunlight to around 0.40 in twilight (Holmes and Smith, 1977b). Holmes and Smith (1977a) suggest that even this relatively small change in the phytochrome photoequilibrium might trigger a response; if a threshold R:FR value is surpassed, or if related to the rate of change in R:FR rather than to the attainment of a specific value. The size of the change found from our measurements was similar; the drop during one day in R:FR between daytime and beginning/end of the day e.g. during July in Helsinki was on average 32 %, and in Gual Pahari it was 28%.

In contrast, Hughes et al. (1984) suggested that even large changes in spectral composition during twilight are not as reliable and accurate as zeitgeber cues for plants reflecting changes in the amount of radiation received over a whole day, especially under plant canopies. Along with spectral photon ratios, we measured PAR photon irradiance which is mainly related to solar elevation angle, clouds and AOD, but not affected by total ozone or water vapour column thickness. Hence, changes in PAR photon irradiance would not be able to convey information related to changes in atmospheric conditions with the accuracy of spectral photon ratios. This brings us back to changes in spectral composition at twilight that, while accepting the caveats from Hughes et al. (1984), could nevertheless hold useful information for plants related to weather conditions and seasonal changes, which would be detected by PHY A or PHY B via changes in FR and the R:FR photon ratio respectively.

Are plants able to differentiate between changes in R:FR ratio caused by neighbouring plants and those resulting from changes in atmospheric conditions during twilight? The role of FR in making this distinction was specifically considered by Morgan and Smith (1978), comparing the effects on stem extension in *Chenopodium album* of continuous, daytime, and end-of-day (EOD) regimes of supplemental FR light. The spectral photon ratio during daytime was concluded to be more important than the EOD-R:FR ratio in determining stem extension in *C. album*. Results from experimental manipulations of R:FR in canopies of the grass *Lolium multiflorum* also suggest that plants are really able to differentiate between changes in R:FR ratio caused by neighbouring plants and those during twilight(Casal et al., 1990). In

addition, Sellaro et al. (2018) recently suggested that phyB-mediated perception of light signals from neighbouring vegetation (not yet creating full shade) and the ability of phyB to act as a temperature sensor occur in different prevailing environmental conditions.

We present evidence that spectral photon ratios can vary substantially during the day, depending on cloudiness, and that the R:FR photon ratio is larger during days with higher atmospheric water vapour. Notably, an average value of 1.15 for the R:FR ratio during the day as suggested by Smith (1982) and other generalizations used (Franklin and Whitelam, 2005; Taulavuori et al., 2010), are not entirely consistent with our measurements, as on average we found that the ratio is above 1.15 for solar elevation angles > 20° during April-September in Helsinki, Finland (1.16-1.28, Table 2) and during May−-September in Gual Pahari, India (1.22-1.40, Table 2). This suggests that the generalization that the R:FR photon ratio remains around a specific narrow range during daytime should be avoided when interpreting plant responses. Moreover, the pattern of changes in R:FR ratio is different when the solar elevation angle is low, depending on the water vapour column thickness and cloudiness.

As the annual pattern in water vapour column thickness is quite consistent from year-to-year and between sites (SI Fig. 2A-B), one can speculate that the R:FR photon ratio may not only be a cue carrying information about neighbouring plants but also for changing seasons and weather conditions, at least in temperate and sub-tropical regions. An additional factor controlling the R:FR photon ratio at high latitudes is the total ozone column thickness, so this could also play a role as an extra seasonal cue (for yearly trends of total ozone column see SI Fig. 7A-B).

### 4.4. Considerations for future research

The patterns of variation in spectral irradiance and photon ratios at ground level that we describe here suggest that future research into the role of specific photon ratios in plant growth, ecophysiology and phenology should be designed using appropriate values for these photon ratios, specific to conditions at the location, season, and time of day relevant to each study. We suggest that future studies should investigate possible effects of varying B:G and B:R photon ratios on terrestrial plants, as these ratios are especially affected by solar elevation angle and could serve as cues related to the diurnal cycle and length of the twilight period, and thus provide organisms with information about the seasons. Most studies about the phenological responses of trees to temperature and photoperiod have overlooked the influence of spectral composition on these processes and how it changes seasonally. A recent review (Brelsford et al., 2019) and study by Chiang et al. (2019) highlight the importance of further investigating the adaptive role of spectral composition as a cue for timing phenology, particularly at high latitudes. The role of blue light in this context has been considered by Molmann et al. (2006), Opseth et al. (2016), Brelsford and Robson, (2018) and Brelsford et al. (2019). Before sunrise, the R:FR photon ratio could serve as cue for adjustment of pre-dawn stomatal opening related to the water vapour column and clouds (Holmes and Klein, 1985).

Finally, spectral cues conveyed through photon ratios might play a role in predictions of plant and ecosystem response to climate change. Modelled climate scenarios predict that increasing global temperatures will result in increased atmospheric water vapour and concomitant changes in the hydrological cycle (IPCC, 2012; Solomon et al., 2009). Given that water vapour has a large effect on spectral irradiance, especially on the R:FR photon ratio, experiments dealing with future climates should take this increase into account. In principle, data from weather and climate models are available on ozone column thickness, water vapour and aerosol optical depth, e.g., from European Centre for Medium-Range Weather Forecasts (ECMWF) Copernicus Service. These data are not as accurate as actual measurements, but on the other hand they are easy to apply and use for any location across the globe. Clouds are well known to be very important modifiers of climate, but the simulation of clouds in climate models is still a work-in-progress. The development of proxy models for relevant photon ratios as a function of solar elevation angle and atmospheric factors would facilitate the interpretation of results from past, present and future field studies of plants and vegetation, while a climatology of the spectral irradiance at ground level could guide the design of controlled environments for plant cultivation.

## Declaration of Competing Interest

The authors declare that they have no known competing financial interests or personal relationships that could have appeared to influence the work reported in this paper.

## Acknowledgements

We thank the principal investigator Gerrit Leeuw and his staff at the Finnish Meteorological Institute for establishing and maintaining the AERONET sites (Helsinki, Finland and Gual Pahari, India) used in this investigation. We thank Julia Krasensky-Wrzaczek for her useful comments on a draft of this manuscript. This work was funded by Academy of Finland (decisions 324555 and 304519 to TMR).

## Supplementary materials

Supplementary material associated with this article can be found, in the online version, at doi:10.1016/j.agrformet.2020.108041.

## References

Aphalo, P.J., 2017. Quantification of UV Radiation, in: UV-B Radiation and Plant Life: Molecular Biology to Ecology. CAB International 10–22.
Aphalo, P.J., 2015. The r4photobiology suite. UV4Plants Bull 1, 21–29. https://doi.org/10.19232/uv4pb.2015.1.14.
Aphalo, P.J., Albert, A., Mcleod, A.R., Robson, T.M., Rosenqvist, E., 2012. Beyond the Visible. COST Action FA0906 UV4growth. University of Helsinki, Division of Plant Biology, Helsinki.
Aphalo, P.J., Ballaré, C.L., 1995. On the importance of information-acquiring systems in plant-plant interactions. Funct. Ecol. 9, 5–14.
Aphalo, P.J., Gibson, D., Di Benedetto, A.H., 1991. Responses of growth, photosynthesis, and leaf conductance to white light irradiance and end-of-day red and far-red pulses in *Fuchsia magellanica* Lam. New Phytol 117, 461–471.
Aphalo, P.J., Robson, T.M., Piiparinen, J., 2016. How to check an array spectrometer [WWW Document]. URLhttp://uv4plants.org/methods/how-to-check-an-array-spectrometer/(accessed 12.7.17).
Bais, A.F., Lucas, R.M., Bornman, J.F., Williamson, C.E., Sulzberger, B., Austin, A.T., Wilson, S.R., Andrady, A.L., Bernhard, G., McKenzie, R.L., Aucamp, P.J., Madronich, S., Neale, R.E., Yazar, S., Young, A.R., de Gruijl, F.R., Norval, M., Takizawa, Y., Barnes, P.W., Robson, T.M., Robinson, S.A., Ballaré, C.L., Flint, S.D., Neale, P.J., Hylander, S., Rose, K.C., Wängberg, S.-Å., Häder, D.-P., Worrest, R.C., Zepp, R.G., Paul, N.D., Cory, R.M., Solomon, K.R., Longstreth, J., Pandey, K.K., Redhwi, H.H., Torikai, A., Heikkilä, A.M., 2018. Environmental effects of ozone depletion, UV radiation and interactions with climate change: UNEP Environmental Effects Assessment Panel, update 2017. Photochem. Photobiol. Sci 17, 127–179.
Ballaré, C.L., 1999. Keeping up with the neighbours: Phytochrome sensing and other signalling mechanisms. Trends Plant Sci 4, 97–102. https://doi.org/10.1016/S1360-1385(99)01383-7.
Ballare, C.L., Senchez, R.A., Scopel, A.L., Casal, J.J., Ghersa, C.M., 1987. Early detection of neighbouring plant by phytochlome perception of spectral changes in reflected light. Plant. Cell Environ. 10, 551–557.
Blumthaler, M., Gröbner, J., Egli, L., Nevas, S., 2013. A guide to measuring solar UV spectra using array spectroradiometers. AIP Conf. Proc. 1531, 805–808. https://doi.org/10.1063/1.4804892.
Brelsford, C.C., 2016. Radiative transfer theory and modelling with libRadtran. UV4Plants Bull 45–50. https://doi.org/10.19232/uv4pb.2016.2.15.
Brelsford, C.C., Nybakken, L., Kotilainen, T.K., Robson, T.M., 2019. The influence of spectral composition on spring and autumn phenology in trees. Tree Physiol 39, 925–950. https://doi.org/10.1093/treephys/tpz026.
Brelsford, C.C., Robson, T.M., 2018. Blue light advances bud burst in branches of three deciduous tree species under short-day conditions. Trees - Struct. Funct. 32, 1157–1164. https://doi.org/10.1007/s00468-018-1684-1.
Casal, J.J., 2013. Photoreceptor signaling networks in plant responses to shade. Annu. Rev. Plant Biol. 64, 403–427.
Casal, J.J., Sanchez, R.., Gibson, D., 1990. The significance of changes in the red / far- red ratio, associated with either neighbour plants or twilight, for tillering in *Lolium multi forum* Lam. New Phytol 116, 565–572.
Chamovitz, D.A., 2018. Plants are intelligent; now what? Nat. Plants 4, 622–623.
Chang, F.L., Li, Z., 2005. A near-global climatology of single-layer and overlapped clouds and their optical properties retrieved from Terra/MODIS data using a new algorithm. J. Clim. 18, 4752–4771. https://doi.org/10.1175/JCLI3553.1.

Chelle, M., Evers, J.B., Combes, D., Varlet-Grancher, C., Vos, J., Andrieu, B., 2007. Simulation of the three-dimensional distribution of the red:far-red ratio within crop canopies. New Phytol 176, 223–234. https://doi.org/10.1111/j.1469-8137.2007.02161.x.

Chia, P., Kubota, C., 2010. End-of-day far-red light quality and dose requirements for tomato rootstock hypocotyl elongation. HortScience 45, 1501–1506.

Chiang, C., Olsen, J.E., Basler, D., Bånkestad, D., Hoch, G., 2019. Latitude and weather influences on sun light quality and the relationship to tree growth. Forests 10, 1–12.

Dahlback, A., Stamnes, K., 1991. A new spherical model for computing the radiation field available for photolysis and heating at twilight. Planet. Space Sci. 39, 671–683. https://doi.org/10.1016/0032-0633(91)90061-E.

Emde, C., Buras-Schnell, R., Kylling, A., Mayer, B., Gasteiger, J., Hamann, U., Kylling, J., Richter, B., Pause, C., Dowling, T., Bugliaro, L., 2016. The libRadtran software package for radiative transfer calculations (version 2.0.1). Geosci. Model Dev. 9, 1647–1672. https://doi.org/10.5194/gmd-9-1647-2016.

Fauchez, T., Arney, G., Kopparapu, R.K., Goldman, D.S., 2018. Explicit cloud representation in the Atmos 1D climate model for Earth and rocky planet applications. AIMS Geosci 4, 180–191. https://doi.org/10.3934/geosci.2018.4.180.

Flint, S.D., Caldwell, M.M., 1998. Solar UV-B and visible radiation in tropical forest gaps: measurements partitioning direct and diffuse radiation. Glob. Chang. Biol. 4, 863–870.

Folta, K.M., Maruhnich, S.A., 2007. Green light: A signal to slow down or stop. J. Exp. Bot. 58, 3099–3111. https://doi.org/10.1093/jxb/erm130.

Franklin, K.A., Whitelam, G.C., 2005. Phytochromes and shade-avoidance responses in plants. Ann. Bot. 96, 169–175. https://doi.org/10.1093/aob/mci165.

Gates, D.M., 1966. Spectral distribution of solar radiation at the Earth's surface. Science 151, 523–529.

Goldberg, B., Klein, W.H., 1977. Variations in the spectral distribution of daylight at various geographical locations on the earth's surface. Sol. Energy 19, 3–13. https://doi.org/10.1016/0038-092X(77)90083-4.

Górski, T., 1980. Annual cycle of the red and far red radiation. Int. J. Biometeorol. 24, 361–365.

Górski, T., 1976. Red and far red radiation at sunset - Annual cycle and dependence on precipitable water. Naturwissenschaften 63, 530–531. https://doi.org/10.1007/BF00596854.

Goyal, A., Szarzynska, B., Fankhauser, C., 2013. Phototropism: At the crossroads of light-signaling pathways. Trends Plant Sci 18, 393–401. https://doi.org/10.1016/j.tplants.2013.03.002.

Grant, R.H., Apostol, K., Gao, W., 2005. Biologically effective UV-B exposures of an oak-hickory forest understory during leaf-out. Agric. For. Meteorol. 132, 28–43. https://doi.org/10.1016/j.agrformet.2005.06.008.

Groemping, U., 2006. Relative importance for linear regression in R: the package relaimpo. J. Stat. Softw. 17, 139–147. https://doi.org/10.18637/jss.v017.i01.

Hernández, R., Kubota, C., 2014. Growth and morphological response of cucumber seedlings to supplemental red and blue photon flux ratios under varied solar daily light integrals. Sci. Hortic. 173, 92–99. https://doi.org/10.1016/j.scienta.2014.04.035.

Holmes, M.G., Klein, W.H., 1985. Evidence for phytochrome involvement in light-mediated stomatal movement in *Phaseolus vulgaris* L. Planta 166, 348–353.

Holmes, M.G., Smith, H., 1977a. The function of phytochrome in the natural environment - II. The influence of vegetation canopies on the spectral energy distribution of natural daylight. Photochem. Photobiol. 25, 539–545. https://doi.org/10.1111/j.1751-1097.1977.tb09125.x.

Holmes, M.G., Smith, H., 1977b. The function of phytochrome in the natural environment - I. Characterization of daylight for studies in photomorphogenesis and photoperiodism. Photochem. Photobiol. 25, 533–538.

Hughes, J.E., Morgan, D.C., Lambton, P.A., Black, C.R., Smith, H., 1984. Photoperiodic time signals during twilight. Plant. Cell Environ 7, 269–277. https://doi.org/10.1111/1365-3040.ep11589464.

Hulburt, E.O., 1953. Explanation of the brightness and color of the sky, particularly the twilight sky. J. Opt. Soc. Am. 43, 113–118. https://doi.org/10.1364/JOSA.43.000805.

IGBP, 1992. Improved global data for land applications. IGBP Global Change Report no. 20, International Geosphere–Biosphere Programme, Stockholm.

IPCC, 2014. Climate change 2014: Synthesis report. Contribution of working groups I, II and III to the fifth assessment report of the Intergovernmental Panel on Climate Change.

IPCC, 2012. Near-term Climate Change: Projections and Predictability. Notes 953–1028. 10.1017/CBO9781107415324.023.

Johnson, T.B., Salisbury, F.B., Connor, G.I., 1967. Ratio of blue to red light: a brief increase following sunset. Science 155, 1663–1665.

Kållberg, P.., Berrisford, P., Hoskins, B.J., Simmons, A., Uppala, S., Lamy-Thépaut, S., Hine, R., 2005. ERA-40 Atlas. Shinfield Park, Reading.

Kärhä, P., Mes, J., Pulli, T., Schreder, J., Partosoebroto, A., Hülsen, G., Askola, J., Gröbner, J., 2014. Improved diffusers for spectroradiometers measuring solar irradiance. UVNews, pp. 25–27.

Kotilainen, T., Lindfors, A., Tegelberg, R., Aphalo, P.J., 2011. How realistically does outdoor UV-B supplementation with lamps reflect ozone depletion: An assessment of enhancement errors. Photochem. Photobiol. 87, 174–183. https://doi.org/10.1111/j.1751-1097.2010.00843.x.

Kotilainen, T., Tegelberg, R., Julkunen-Tiitto, R., Lindfors, A., Aphalo, P.J., 2008. Metabolite specific effects of solar UV-A and UV-B on alder and birch leaf phenolics. Glob. Chang. Biol. 14, 1294–1304. https://doi.org/10.1111/j.1365-2486.2008.01569.x.

Kylling, A., Albold, A., Seckmeyer, G., 1997. Transmittance of a cloud is wavelength-dependent in the UV-range: Physical interpretation. Geophys. Res. Lett. 24, 397–400. https://doi.org/10.1029/97GL00111.

Lee, D.W., Downum, K.R., 1991. The spectral distribution of biologically active solar radiation at Miami, Florida, USA. Int. J. Biometeorol 35, 48–54.

Lindeman, R.H., Merenda, P.F., Gold, R.Z., 1980. Introduction to bivariate and multivariate analysis. Scott, Foresman, Glenview, IL.

Lindfors, A., Arola, A., 2008. On the wavelength-dependent attenuation of UV radiation by clouds. Geophys. Res. Lett. 35, 1–5. https://doi.org/10.1029/2007GL032571.

Lindfors, A., Heikkilä, A., Kaurola, J., Koskela, T., Lakkala, K., 2009. Reconstruction of solar spectral surface UV irradiances using radiative transfer simulations. Photochem. Photobiol. 85, 1233–1239. https://doi.org/10.1111/j.1751-1097.2009.00578.x.

Mayer, B., Kylling, A., 2005. Technical note: The libRadtran software package for radiative transfer calculations – description and examples of use. Atmos. Chem. Phys. 5, 1855–1877.

Mølmann, J.A., Junttila, O., Johnsen, Ø., Olsen, J.E., 2006. Effects of red, far-red and blue light in maintaining growth in latitudinal populations of Norway spruce (*Picea abies*). Plant, Cell Environ 29, 166–172. https://doi.org/10.1111/j.1365-3040.2005.01408.x.

Morales, L.O., Brosché, M., Vainonen, J., Jenkins, G.I., Wargent, J.J., Sipari, N., Strid, Å., Lindfors, A.V, Tegelberg, R., Aphalo, P.J., 2013. Multiple roles for UV RESISTANCE LOCUS8 in regulating gene expression and metabolite accumulation in Arabidopsis under solar ultraviolet radiation. Plant Physiol 161, 744–759. https://doi.org/10.1104/pp.112.211375.

Morales, L.O., Tegelberg, R., Brosché, M., Keinänen, M., Lindfors, A., Aphalo, P.J., 2010. Effects of solar UV-A and UV-B radiation on gene expression and phenolic accumulation in *Betula pendula* leaves Effects of solar UV-A and UV-B radiation on gene expression and phenolic accumulation in Betula pendula leaves. Tree Physiol 30, 923–934. https://doi.org/10.1093/treephys/tpq051.

Morgan, D.C., Smith, H., 1978. The relationship between phytochrome photoequilibrium and development in light grown *Chenopodium album* L. Planta 193, 187–193.

Nilsen, J., 1985. Light climate in northern areas. In: Junttila, O., Nilsen, J. (Eds.), Plant Production in the North. Norwegian University Press, pp. 62–72.

Okata, M., Nakajima, T., Suzuki, K., Inoue, T., Nakajima, T.Y., Okamoto, H., 2017. A study on radiative transfer effects in 3-D cloudy atmosphere using satellite data. J. Geophys. Res. Atmos. 122, 443–468. https://doi.org/10.1002/2016JD025441. Received.

Opseth, L., Holefors, A., Rosnes, A.K.R., Lee, Y.K., Olsen, J.E., 2016. FTL2 expression preceding bud set corresponds with timing of bud set in Norway spruce under different light quality treatments. Environ. Exp. Bot. 121, 121–131. https://doi.org/10.1016/j.envexpbot.2015.05.016.

R Core Team, 2017. R: A Language and Environment for Statistical Computing.

Seckmeyer, G., Erb, R., Albold, A., 1996. Transmittance of a cloud is wavelength-dependent in the UV-range. Geophys. Res. Lett. 23, 2753–2755.

Seckmeyer, G., Pissulla, D., Glandorf, M., Henriques, D., Johnsen, B., Webb, A., Siani, A.M., Bais, A., Kjeldstad, B., Brogniez, C., Lenoble, J., Gardiner, B., Kirsch, P., Koskela, T., Kaurola, J., Uhlmann, B., Slaper, H., Den Outer, P., Janouch, M., Werle, P., Gröbner, J., Mayer, B., De La Casiniere, A., Simic, S., Carvalho, F, 2008. Variability of UV irradiance in Europe. Photochem. Photobiol. 84, 172–179. https://doi.org/10.1111/j.1751-1097.2007.00216.x.

Sellaro, R., Crepy, M., Trupkin, S.A., Karayekov, E., Buchovsky, A.S., Rossi, C., Casal, J.J., 2010. Cryptochrome as a sensor of the blue/green ratio of natural radiation in Arabidopsis. Plant Physiol 154, 401–409. https://doi.org/10.1104/pp.110.160820.

Sellaro, R., Smith, R.W., Legris, M., Fleck, C., Casal, J.J., 2018. Phytochrome B dynamics departs from photoequilibrium in the field. Plant. Cell Environ. https://doi.org/10.1111/pce.13445.

Serrano, D., Núñez, M., Utrillas, M.P., Marín, M.J., Marcos, C., Martínez-Lozano, J.A., 2014. Effective cloud optical depth for overcast conditions determined with a UV radiometers. Int. J. Climatol. 34, 3939–3952. https://doi.org/10.1002/joc.3953.

Smith, H., 1982. Light quality, photoperception and plant strategy. Annu. Rev. Plant Physiol. 33, 481–518.

Solomon, S., et al., 2009. Irreversible climate change due to carbon dioxide emissions. Proc. Natl. Acad. Sci 106, 1704–1709.

Stamnes, K., Tsay, S.-C., Wiscombe, W., Jayaweera, K., 1988. Numerically stable algorithm for discrete-ordinate-method radiative transfer in multiple scattering and emitting layered media. Appl. Opt. 27, 2502–2509. https://doi.org/10.1364/AO.27.002502.

Taulavuori, K., Sarala, M., Taulavuori, E., 2010. In: Lüttge, U., Beyschlag, W., Büdel, B., Francis, D. (Eds.), Growth responses of trees to Arctic light environment. Progress in Botany, pp. 157–168. https://doi.org/10.1007/978-3-642-38797-5.

Vince-Prue, D., Clapham, D., Ekberg, I., Norell, L., 2001. Circadian timekeeping for the photoperiodic control of budset in *Picea abies* (Norway spruce) seedlings. Biol. Rhythm 32, 479–487. https://doi.org/10.1076/brhm.32.4.479.1336.

Welling, A., Palva, E.., 2006. Molecular control of cold acclimation in trees. Physiol. Plant. 127, 167–181. https://doi.org/10.1111/j.1399-3054.2006.00672.x.

Wickham, H., 2016. Elegant graphics for data analysis. Springer-Verlag, New York.

Wilke, C.O., 2018. ggridges: Ridgeline Plots in “ggplot2.”.

Yang, Z., Kubota, C., Chia, P., Kacira, M., 2012. Effect of end-of-day far-red light from a movable LED fixture on squash rootstock hypocotyl elongation. Sci. Hortic. 136, 81–86. https://doi.org/10.1016/j.scienta.2011.12.023.

Ylianttila, L., Visuri, R., Huurto, L., Jokela, K., 2005. Evaluation of a single-monochromator diode array spectroradiometer for sunbed UV-radiation measurements. Photochem. Photobiol. 81, 333–341. https://doi.org/10.1562/2004-06-02-RA-184.